

Small or medium-scale focused research project (STREP)

ICT Call 5

FP7-ICT-2009-5

NEW ELECTRONICS CONCEPT: WAFER-SCALE EPITAXIAL GRAPHENE

ConceptGraphene

**Deliverable report.**

**Deliverable 3.3:** *Report on metrological measurements on the Prototype QHR standard, prototype #1*

Nature of the deliverable: **R** = Report

Dissemination level: **PU** = Public.

Lead Partner: **3** = National Physical Laboratory

Delivery date: month 24 of the project

## **Executive summary**

In this report we present a detailed description of the metrological characterization of graphene device #1, including an explanation of the measurement system, data analysis and the uncertainty budget which underpins the result. Metrological characterisation was performed according to “Revised technical guidelines for reliable dc measurements of the quantized Hall resistance” [1].

### **Contributors and their input:**

Epitaxial graphene was grown by partner **6** – Linköping University

Devices were patterned by partner **1** – Chalmers University

Magnetotransport measurements were carried out by partner **3** – NPL

Theory was developed by partner **5** – Lancaster University

Data were analysed by partners **1 & 5**

Report written by all contributors

## The sample

Graphene was grown by partner 6 on the Si face of 4H-silicon carbide (Epi-SiC) [2]. Hall bars (160  $\mu\text{m}$  long and 35  $\mu\text{m}$  wide) (

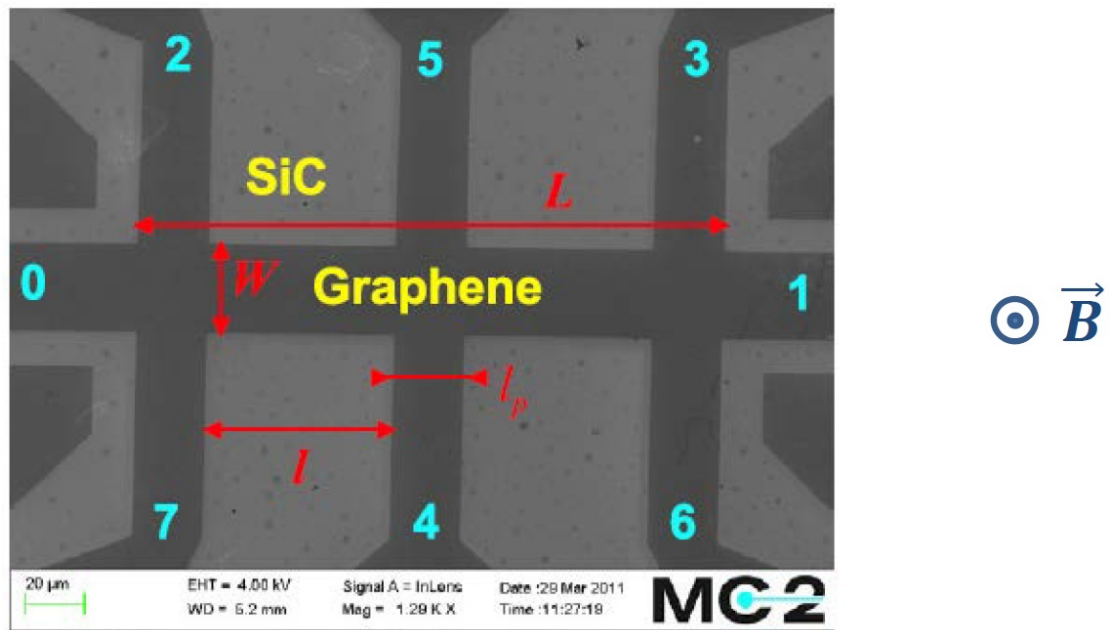


Figure 1) were patterned by partner 1 using standard electron beam lithography. The as-grown graphene was electron-doped to  $n=1.1 \times 10^{12} \text{ cm}^{-2}$  as a result of charge transfer from the substrate [3]. The sample was then encapsulated with the polymer bilayer COP/ZEP520A to improve temporal stability and doping homogeneity of the sample, and exposed to Deep UV to tune the carrier concentration [4]. Half-integer Quantum Hall effect observed in this sample confirmed its monolayer nature [5].

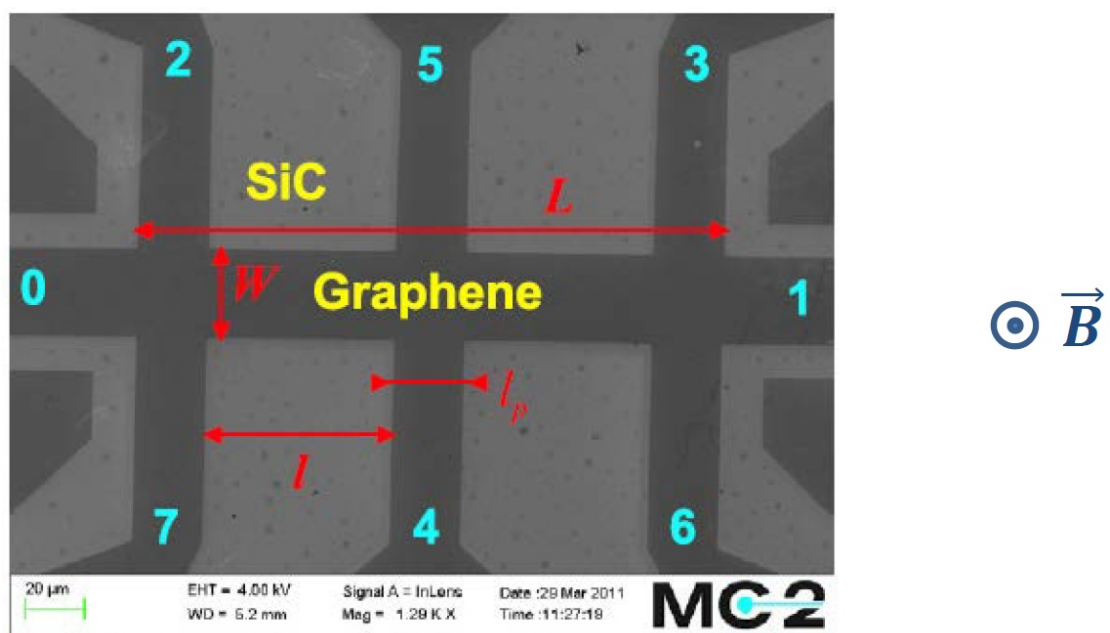
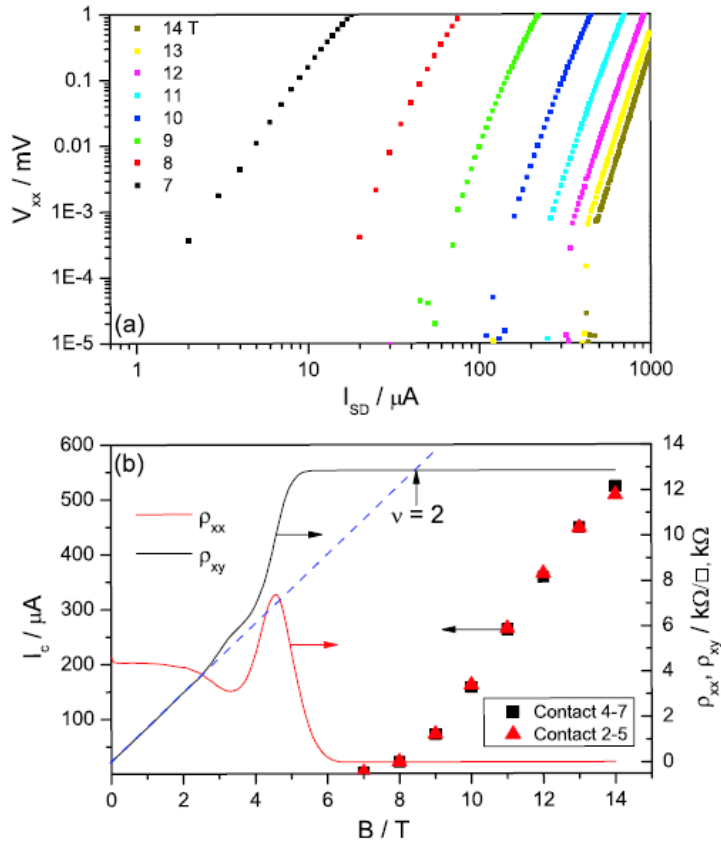


Figure 1. SEM image of the sample.

### Determination of the quantum Hall breakdown current

Accurate quantum Hall resistance measurements require that the longitudinal voltage remains zero to ensure the device is in the non-dissipative state, which can be violated by the breakdown of the QHE at high source–drain current levels. Figure 2(a) shows the determination of the breakdown current  $I_c$  for different values of  $B$  along the  $\nu = 2$  plateau marked in Figure 2(b). Here we define  $I_c$  as the source–drain current,  $I_{sd}$ , at



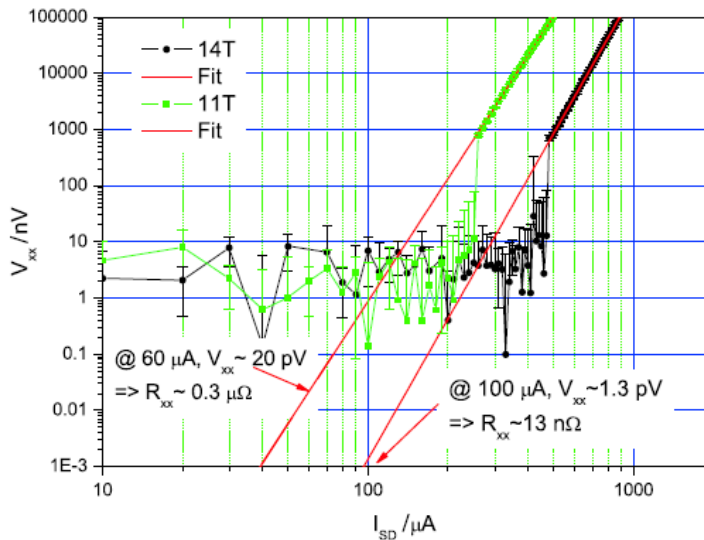
which

Figure 2. (a) Measurement of  $V_{xx}$  (contacts 4 and 7) as a function of source–drain current at different values of magnetic flux density ranging from  $B = 7$  T (left hand curve) to 14 T (right curve) in steps of 1 T. (b) Transverse ( $\rho_{xy}$ ) (contacts 4 and 5) and longitudinal ( $\rho_{xx}$ ) (contacts 4 and 7) resistivity measurement at the reduced carrier density of  $4.6 \times 10^{11} \text{ cm}^{-2}$  measured at  $I_{sd} = 1 \mu\text{A}$  together with the measured breakdown current,  $I_c$ . Dashed blue line indicates position of the exact  $\nu = 2$  filling factor for the low field carrier density.

$V_{xx}$  exceeds 100 nV. Above the breakdown current the voltage increases rapidly as a function of current as a consequence of the sudden increase in electron temperature

and subsequent increase in longitudinal resistivity [6]. In Figure 2(b) the values of the breakdown current are plotted as a function of  $B$  together with  $\rho_{xx}$  and  $\rho_{xy}$ .

Figure 3 shows the measurement of  $V_{xx}$  as a function of  $I_{sd}$  at 11 T and 14 T in more detail (these are the magnetic flux densities at which the precision resistance measurements were later performed). On the log–log plot it is clear that above the breakdown current the longitudinal voltage shows a power law dependence on current. The red lines in the figure are a fit to this part of the trace. For the highest flux density of 14 T the breakdown current is  $\sim 500 \mu\text{A}$ ; however, the maximum source–drain current used in our precision measurements is  $100 \mu\text{A}$ . The extrapolated fitted line indicates that the expected  $V_{xx}$  is  $\sim 1.3 \text{ pV}$  at  $100 \mu\text{A}$  and therefore  $R_{xx} \approx 13 \text{ n}\Omega$ . Note that in the immediate vicinity of the breakdown current  $V_{xx}$  drops away much more quickly than this power-law behaviour before it disappears in the noise of the DVM ( $\pm 5 \text{ nV}$ ) (the shape of the breakdown curve is remarkably similar to that observed by Cage et al [7] for GaAs heterostructure devices) and therefore the  $R_{xx} \approx 13 \text{ n}\Omega$  is the upper bound. On the basis of this analysis we can be confident that the longitudinal resistivity is vanishingly small and that there is a considerable margin on  $I_{sd}$  in our experiments. A few measurements were performed at a lower magnetic flux density around 11 T. For these measurements a lower  $I_{sd}$  of  $60 \mu\text{A}$  was chosen and a similar extrapolation of the high source–drain currents gives  $V_{xx} \approx 20 \text{ pV}$  and  $R_{xx} \approx 0.3 \mu\Omega$  again as the upper bound.



**Figure 3.** Log–log plot of  $V_{xx}$  as a function of source–drain current at 11 T (green squares) and 14 T (black dots). The red lines are fits to the data at high source–drain currents. 5 nV is the noise floor of the voltmeter.

## Contact resistance

For accurate quantum Hall measurements it is important that the contact resistance is well below  $\approx 100 \Omega$  [8]. The contact resistance has been measured in the field and current range, where  $R_{xx}$  is vanishingly small, using the three-terminal measurement technique. For instance, to evaluate the resistance of the drain contact (0 in Figure 1), the measuring current ( $I_{sd}$ ) was passed through contacts 0 and 1 and the potential difference between contacts 0 and, for instance, 2, 3 or 5 is measured. The second contact used (i.e., 2, 3 or 5) is a contact at the same nominal potential as the contact under test (here 0), taking into account the direction of the magnetic flux density vector  $B$ .

On the pristine devices all contact resistances were below  $1 \Omega$ , however, after a dozen thermal cycles between 300 mK and room temperature and several re-bondings to the TO8-header resulting in damage to some of the bonding pads, some of the contacts acquired higher resistance. These final values are summarised in Table 1, which demonstrates that the condition on the contact resistance to be under  $100 \Omega$  was still satisfied for most of the contacts.

**Table 1. Three-terminal contact resistances measured at  $B = 14 \text{ T}$  in the  $\nu = 2$  quantum Hall state. The measurement current was  $10 \mu\text{A}$  and a lead resistance of  $2.7 \Omega$  was subtracted.**

Contact no	R/ $\Omega$
0	0.3
1	0.3
2	15
3	125
4	0.3
5	90
6	23
7	0.3

## Robustness of the Quantum Hall Effect

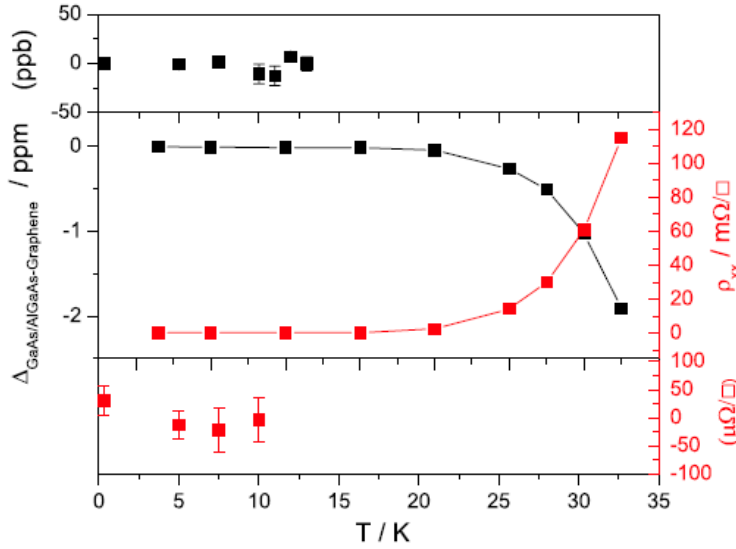


**Figure 4. Middle:** measurement of  $\Delta_{\text{GaAs/AlGaAs-graphene}} = [R_{\text{H}}(\text{GaAs/AlGaAs}, T = 1.5 \text{ K}) - R_{\text{H}}(\text{graphene}, T)]/(R_{\text{K}}/2)$  and  $\rho_{xx}$  as a function of temperature for the graphene device.  $B = 14 \text{ T}$  for the graphene device and  $10.5 \text{ T}$  for the GaAs/AlGaAs device. The measurement current was  $60 \text{ } \mu\text{A}$ . **Top and bottom:** high-resolution measurements of  $\Delta_{\text{GaAs/AlGaAs-graphene}}$  and  $\rho_{xx}$  demonstrating ppb-level quantization. For the middle panel the carrier density was  $4.6 \times 10^{11} \text{ cm}^{-2}$  and for the top and bottom panels the density was  $6.7 \times 10^{11} \text{ cm}^{-2}$ .

Figure 4 demonstrates the robustness of the  $\nu = 2$  quantum Hall state as a function of temperature. Here  $\Delta_{\text{GaAs/AlGaAs-graphene}} = [R_{\text{H}}(\text{GaAs/AlGaAs}, T = 1.5 \text{ K}) - R_{\text{H}}(\text{graphene}, T)]/(R_{\text{K}}/2)$  quantifies the difference between the graphene sample and a fixed reference GaAs/AlGaAs device. In a separate measurement the longitudinal resistivity was measured for the graphene device and plotted in the same graph. The temperature for the reference device is held constant at  $1.5 \text{ K}$  while the temperature for the graphene device is varied. The middle panel of Figure 4 shows a low resolution measurement across a wide temperature range and demonstrates that  $R_{\text{H}}$  starts to deviate as soon as a measurable  $\rho_{xx}$  appears. The top and bottom panels are high-resolution measurements which demonstrate ppb-level quantization up to  $15 \text{ K}$  when  $\rho_{xx}$  is of the order of several tens of  $\mu\Omega$  (the high-resolution measurements were performed on an earlier cooldown cycle of the device when the charge carrier density was slightly higher).

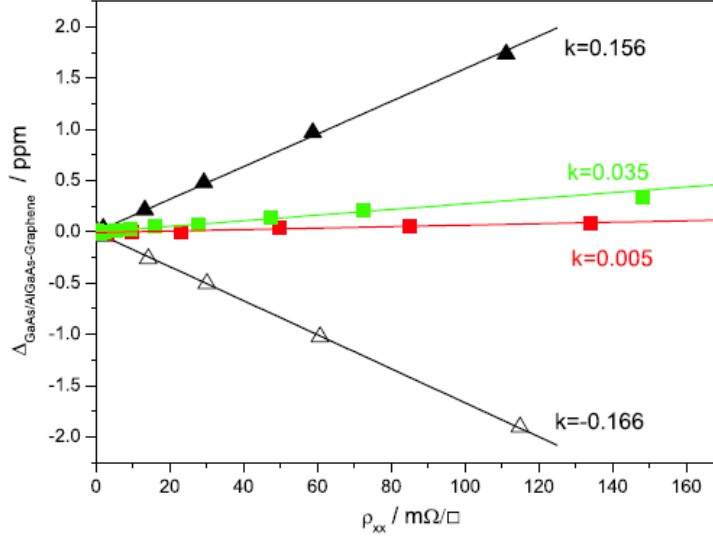


**Figure 5.** Variation of  $\Delta_{\text{GaAs/AlGaAs-graphene}}$  as a function of  $\rho_{xx}$  for three different charge carrier densities determined from data such as displayed in Figure 4. Red =  $9.1 \times 10^{11} \text{ cm}^{-2}$ , green =  $6.7 \times 10^{11} \text{ cm}^{-2}$  and black =  $4.6 \times 10^{11} \text{ cm}^{-2}$ . Open black triangles are measured in reverse field direction. Solid lines are fits to the data.

In Figure 5 we have plotted  $\Delta_{\text{GaAs/AlGaAs-graphene}}$  versus  $\rho_{xx}$  for three separate cooldown cycles of the device. Each time  $\Delta_{\text{GaAs/AlGaAs-graphene}}$  is proportional to  $\rho_{xx}$ , identical to the well-known empirical relationship  $\Delta R_H = k\rho_{xx}$  which has been observed for traditional semiconductor systems [8]. The value of  $k$  varies significantly between different runs which are signified by different charge carrier densities (in between cooldowns the sample was exposed to UV radiation in order to reduce the carrier density in small controllable steps). For the final and lowest charge carrier density we also measured  $k$  in the opposite magnetic field direction. The fact that the sign of  $k$  changes with the  $B$ -field direction indicates that the observed relation between  $R_H$  and  $\rho_{xx}$  is due to inhomogeneity of the charge density in the sample as proposed by van der Wel *et al* [9] rather than the finite width of the voltage probes for which no sign change is expected. In the latter case  $k = l_p/W \approx 0.7$  for both  $B$ -field directions, which is clearly inconsistent with the experimental data. A plausible explanation for the increase in  $k$  with reducing carrier density could be the increase in inhomogeneity in the sample as we get closer to the Dirac point [10]. This is supported by the fact that the value of  $k$  was found to be different for different combinations of measurement contacts (not shown). Combining the results from Figure 3, where we estimated  $R_{xx}$ , with the value of  $k$  obtained in Figure 5 allows us to estimate the expected relative error in  $R_H$ . For  $B$

= 14 T and  $I_{sd} = 100 \mu\text{A}$  we obtained  $R_{xx} = 13 \text{ n}\Omega$ , which with  $k = 0.16$  implies that we can expect a relative error in  $R_H$  much less than  $10^{-12}$ . Similarly for  $60 \mu\text{A}$  at  $B = 11 \text{ T}$  the relative error would be much less than  $10^{-11}$ . In Figure 6 (middle) the same experiment as in Figure 4 is repeated but this time with magnetic flux density as the parameter and  $T = 300 \text{ mK}$ . The magnetic flux density for the reference device is held constant at the centre of the  $\nu = 2$  plateau and the magnetic flux density for the graphene sample is varied. Top and bottom panels are high-resolution measurements which demonstrate ppb-level quantization (again measured on a different cooldown cycle). The graph shows that the  $\nu = 2$  quantum Hall plateau extends over a range of at least 4 T and the measurement is only limited from above by the maximum available magnetic field. The inset is a log-log plot of  $\Delta_{\text{GaAs/AlGaAs-graphene}}$  as a function of  $\rho_{xx}$  similar to Figure 5 and the blue line is  $\Delta R_H = k\rho_{xx}$  with  $k = 0.39$ .

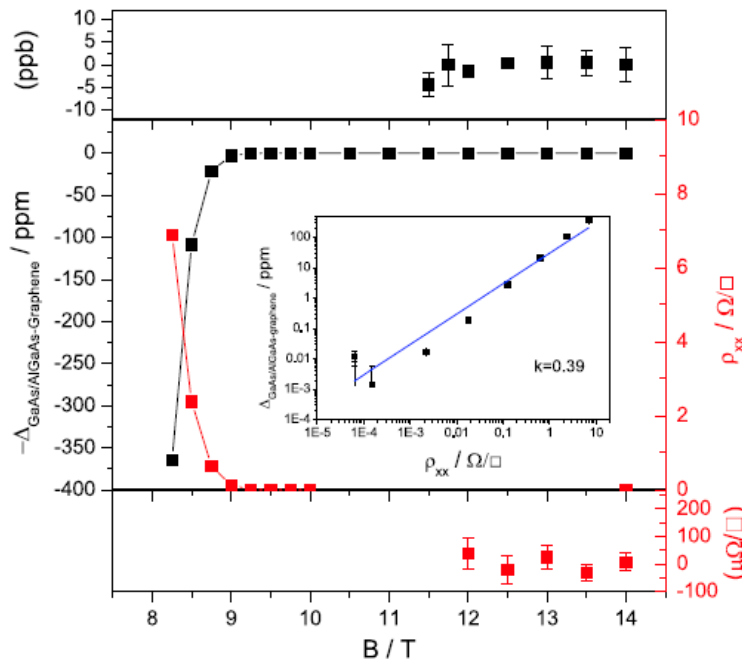


**Figure 6. Middle:** measurement of  $\Delta_{\text{GaAs/AlGaAs-graphene}} = [R_H(\text{GaAs/AlGaAs}, B = 10.5 \text{ T}) - R_H(\text{graphene}, B)] / (R_K/2)$  and  $\rho_{xx}$  as a function of  $B$  on the graphene device.  $T = 0.3 \text{ K}$  for the graphene device and  $1.5 \text{ K}$  for the GaAs/AlGaAs device. The measurement current was  $60 \mu\text{A}$ . **Top and bottom:** high-resolution measurements of  $\Delta_{\text{GaAs/AlGaAs-graphene}}$  and  $\rho_{xx}$  demonstrating ppb-level quantization. For the middle panel the carrier density was  $4.6 \times 10^{11} \text{ cm}^{-2}$  and for the top and bottom panels the density was  $6.7 \times 10^{11} \text{ cm}^{-2}$ . **Inset:** log-log plot of the variation of  $\Delta_{\text{GaAs/AlGaAs-graphene}}$  as a function of  $\rho_{xx}$  for the data in the middle panel.

From the inset it can be seen that the data do not quite follow a linear dependence as might be expected. A likely reason for this deviation is the fact that as a function of  $B$

the charge carrier density in epitaxial graphene is not constant [11], which results in a variation of  $k$  as a function of  $B$ . Comparing the performance of our graphene device with that of GaAs devices shows a significantly wider operational parameter space for the  $\nu = 2$  quantum Hall state. In GaAs the field range is usually a few tenths of a tesla up to 1 T for the best devices and for temperature the operational range is generally below 2 K [8, 12].

### Noise analysis

Precision measurements were made using a cryogenic current comparator (CCC). The principle of operation of the CCC is as follows: Two isolated current sources separately drive current through two samples and through CCC wiring wound in opposition. The current ratio can be set via electronics to a few parts in  $10^6$  and this ratio is improved to a level of a part in  $10^{11}$  by forming a negative feedback loop from the superconducting quantum interference device (SQUID) to one of the current sources. The CCC is topologically equivalent to a superconducting cylinder, the magnetic flux generated by the currents is totally expelled from the CCC due to the Meissner effect and the SQUID is sensing the signal proportional to the difference between the two currents. The feedback loop ensures that the currents are kept at the same value. The voltage on the potential contacts is measured with a low-noise voltmeter and the resistances of the two devices are compared.

Figure 7 shows the Allan deviation for a 3.5 h measurement of graphene against GaAs at  $\nu = 2$ . The measurement data have been analysed in blocks of three intervals consisting of a 1 s settling time plus 10 s data collection interval (for optimum CCC performance) and a 1 s data transfer each to give a value for the resistance ratio every 36 s. (We regularly checked the settling time by varying the wait-time after current reversal and inspecting the measurement result for systematic correlations.) Adding all the known instrumental noise components in quadrature gives a total noise of 8 nV for a 10 s measurement interval. For a measurement current of  $\pm 100 \mu\text{A}$  in  $R_{K,\nu=2}$  this corresponds to a relative deviation of 3 parts in  $10^9$ . From Figure 7 we see that the first data point is also at 4 parts in  $10^9$ , confirming that the overall measurement resolution is consistent with the measured noise. The Allan deviation decreases as  $1/\sqrt{\tau}$  expected for white noise and shows that the current reversal technique efficiently removes the non-white noise. After 3.5 h measurement time a relative uncertainty of 2 parts in  $10^{10}$  is achieved. If the CCCs can be made to operate at their optimum noise performance, a single block of three measurements would give a

relative uncertainty slightly better than 1 part in  $10^9$  and 6 parts in  $10^{11}$  after 3.5 h (blue dot and dashed line in Figure 7).

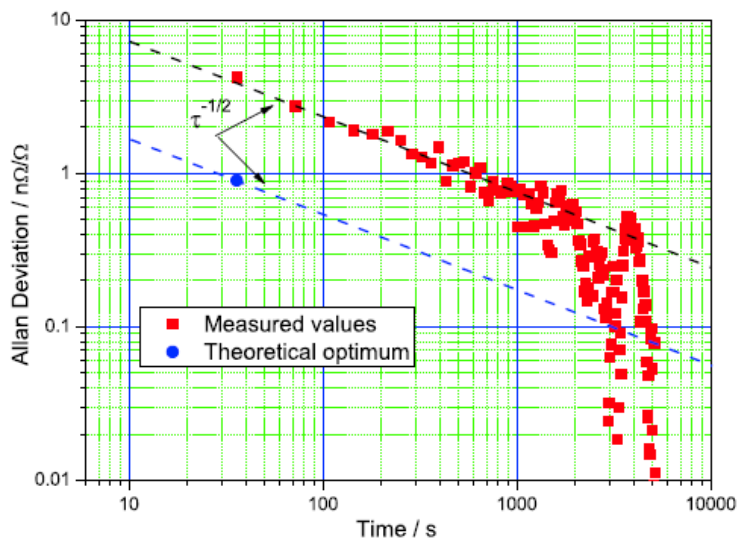


**Figure 7.** Typical Allan deviation of the resistance ratio for a 1 : 1 measurement of graphene against GaAs/AlGaAs heterostructure at  $\nu = 2$  for a measurement current of  $100 \mu\text{A}$ .

### Comparison result

In order to examine the accuracy of resistance quantisation in a test device it has to be compared to a reference device. For most precise comparison, the reference device must also be a quantum Hall device, such as made of GaAs/AlGaAs. Two different QH devices need to be set up at the same quantum Hall plateau so that a one-to-one comparison of resistance can be made (in principle one could also compare different index plateaux if different ratios are available on the CCC). Table summarises the properties of two GaAs/AlGaAs devices, PTB2 and LEP, used in our experiments alongside the graphene sample GR9.

**Table 2.** Device parameters. The dimensions are defined in Figure 1. The contacts on the PTB2 sample were made of small tin balls at the edges of the chip and so voltage probe width is not applicable.

Device	L/mm	W/mm	l/mm	$L_p$ /mm	$\mu/T^{-1}$	$n/10^{11} \text{ cm}^{-2}$
PTB2	6.0	2.5	$\sim 1.5$	N/A	40	4.6
LEP	2.2	0.4	0.5	0.050	50	5.1
GR9	0.16	0.035	0.06	0.024	0.75	4.6

Unfortunately, the quantum Hall plateaux of the graphene and the GaAs/AlGaAs devices do not overlap and two cryostats have to be used for this experiment, one of which was the travelling quantum Hall system of the BIPM. Hartland *et al* [13] used a clever method of tilting one device with respect to the magnetic field direction to make the centres of the plateaux in GaAs and Si occur at the same magnetic field, a trick not currently possible in our quantum Hall probe. Using two cryostats does lead

to an increase in noise and subsequent lengthening of the measurement time. The graphene sample was mounted in a 14 T / 300 mK cryostat and connected to the slave side of the CCC bridge. Two GaAs / AlGaAs samples were mounted in the transportable 11.7 T / 1.5 K cryostat provided by the BIPM and connected to the master side. For the graphene sample the  $B_v=2$  was set to 14 T, our maximum available magnetic field, and either 9.5 T or 10.5 T for samples PTB2 and LEP, respectively. The winding ratio on the bridge was always 1600 : 1600 turns. The red triangles in Figure 8 are the results for GR9 against PTB2 for four different source–drain currents in the devices (using contacts 2 and 7 on the graphene device for  $R_H$  and contacts 4 and 5 on the GaAs device). The pink diamond is a measurement for GR9 against LEP at  $I_{sd} = 50 \mu\text{A}$  (using the same contact configuration as for the red triangle measurements). Here  $\Delta_{\text{GaAs/AlGaAs-graphene}} = [R_H(\text{GaAs/AlGaAs}) - R_H(\text{graphene})]/(R_K/2)$  and each data point consists of an average of between 3 h and 10 h worth of data. The uncertainty increases for lower  $I_{sd}$  because the signal-to-noise ratio is worse for lower  $I_{sd}$ . To eliminate the possibility of errors due to non-zero  $\rho_{xx}$  we repeated a number of these measurements for non-opposite contacts. Note that it is very difficult to measure  $\rho_{xx}$  directly to the required level of precision (see, for example, Figure 3). The green dot is a measurement using contacts 3 and 4 for  $R_H(\text{GaAs/AlGaAs})$  on the PTB2 device at  $I_{sd} = 100 \mu\text{A}$ . The blue square is a measurement using contacts 2 and 4 for  $R_H(\text{graphene})$  on the graphene device at  $I_{sd} = 75 \mu\text{A}$ . Another test to check for small errors is to reverse the direction of magnetic field on the graphene sample. The result of this measurement is represented by the light blue hexagon for  $I_{sd} = 60 \mu\text{A}$  (using the same contact configuration as for the red triangle measurements). Finally, the devices were exchanged between the NPL and BIPM cryostats in order to check for small parasitic leakages (the magnetic field was set to 11.5 T for the graphene device in the BIPM cryostat). This data point is shown as the black square in Figure 8 (using the same contact configuration as for the red triangle measurements). The data in Figure 8 show no sign of any systematic errors in the measurement campaign and so all results can be combined to give a weighted mean of  $\Delta_{\text{GaAs/AlGaAs-graphene}} = (-4.7 \pm 8.6) \times 10^{-11}$ . Combining this with the total type B uncertainty gives  $8.7 \times 10^{-11}$  as the overall uncertainty on the difference between  $R_H(\text{GaAs/AlGaAs})$  and  $R_H(\text{graphene})$ . The uncertainty budget is summarised in Table 3.

**Table 3. Uncertainty budget.**

Contribution	Uncertainty/p $\Omega$ $\Omega^{-1}$
Reproducibility	86
CCC ratio error	11

Leakage	10
Servo error	6
Miscellaneous	<1
Combined standard uncertainty	87

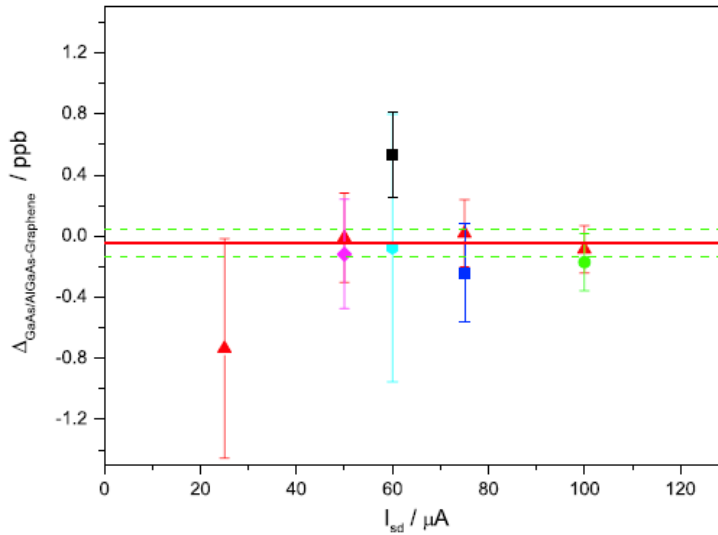


**Figure 8.** Measurement of GaAs/AlGaAs–graphene for the direct comparison of  $R_H(\text{GaAs/AlGaAs})$  and  $R_H(\text{graphene})$  as a function of  $I_{sd}$ . The uncertainty bars represent the  $\pm 1\sigma$  standard deviation of the mean. Different symbols are explained in the text. The red line is the weighted mean of all the data points and the green lines signify  $\pm 1\sigma$ .

## Dissemination

The results of this work have been presented at the Conference on Precision Electromagnetic Measurements, 1-6 July 2012, Washington D.C., USA and will be presented at the ConceptGraphene dissemination workshop at NPL, October 15-16, 2012. A journal article has been published in *Metrologia* [14].

## References:

- 1 F. Delahaye and B. Jeckelmann, *Metrologia* **40**, 217 (2003)
- 2 C. Virojanadara, M. Syvajarvi, R. Yakimova, L. I. Johansson, A. A. Zakharov and T. Balasubramanian, *Phys Rev B* **78**, 245403 (2008).
- 3 S. Kopylov, A. Tzalenchuk, S. Kubatkin and V. I. Fal'ko, *Appl Phys Lett* **97**, 112109 (2010).
- 4 S. Lara-Avila, K. Moth-Poulsen, R. Yakimova, T. Bjornholm, V. Fal'ko, A. Tzalenchuk and S. Kubatkin, *Adv. Mater.* **23**, 878 (2011).
- 5 A. Tzalenchuk, S. Lara-Avila, A. Kalaboukhov, S. Paolillo, M. Syvajarvi, R. Yakimova, O. Kazakova, T. J. B. M. Janssen, V. Fal'ko and S. Kubatkin, *Nat Nanotechnol* **5**, 186 (2010).
- 6 D. Yoshioka *The Quantum Hall Effect* Springer, Berlin (2002)
- 7 M.E. Cage, R.F. Dziuba, B.F. Field, E.R. Williams, S.M. Girvin, A.C. Gossard, D.C. Tsui and R.J. Wagner, *Phys. Rev. Lett.* **51**, 1374 (1983)

- 
- 8 B. Jeckelmann and B. Jeanneret, *Rep. Prog. Phys.* **64**, 1603 (2001)
- 9 W. van der Wel, C.J.P.M. Harmans and J.E. Mooij *J. Phys. C: Solid State Phys.*, **21**, L171 (1988)
- 10 K.S. Novoselov, A.K. Geim, S.V. Morozov, D. Jiang, M.I. Katsnelson, I.V. Grigorieva, S.V. Dubonos and A.A. Firsov, *Nature* **438**, 197–200 (2005)
- 11 T.J.B.M. Janssen, A. Tzalenchuk, R. Yakimova, S. Kubatkin, S. Lara-Avila, S. Kopylov and V.I. Fal'ko, *Phys. Rev. B* **83**, 233402 (2011)
- 12 W. Poirier and F. Schopfer *Eur. Phys. J.—Special Topics* **172**, 207 (2009)
- 13 A. Hartland, K. Jones, J.M. Williams, B.L. Gallagher and T. Galloway, *Phys. Rev. Lett.* **66**, 969 (1991)
- 14 T.J.B.M. Janssen, J.M. Williams, N.E. Fletcher, R. Goebel, A. Tzalenchuk, R. Yakimova, S. Lara-Avila, S. Kubatkin and V.I. Fal'ko, *Metrologia* **49**, 294 (2012)